

Immune cellular patterns of distribution affect outcomes of patients with non-small cell lung cancer

Edwin Roger Parra (✉ ERParra@mdanderson.org)

The University of Texas MD Anderson Cancer Center <https://orcid.org/0000-0001-9068-1636>

Jiexin Zhang

<https://orcid.org/0000-0001-9526-6730>

Mei Jiang

The University of Texas MD Anderson Cancer Center, Houston, Texas

Auriole Tamegnon

The University of Texas MD Anderson Cancer Center

Renganayaki Pandurengan

The University of Texas MD Anderson Cancer Center

Carmen Behrens

The University of Texas MD Anderson Cancer Center

John Heymach

The University of Texas MD Anderson Cancer Center <https://orcid.org/0000-0001-9068-8942>

Cesar Moran

The University of Texas MD Anderson Cancer Center <https://orcid.org/0000-0003-1158-5713>

J. Jack Lee

The University of Texas M D Anderson Cancer Center <https://orcid.org/0000-0001-5469-9214>

Don Gibbons

The University of Texas MD Anderson Cancer Center <https://orcid.org/0000-0003-2362-3094>

Ignacio Wistuba

The University of Texas MD Anderson Cancer Center

Article

Keywords: Immune cells, immune checkpoints, myeloid-derived suppressor cell, marker co-expression, non-small cell lung cancer, computational image analysis

Posted Date: June 24th, 2022

DOI: <https://doi.org/10.21203/rs.3.rs-1755739/v1>

License:  This work is licensed under a Creative Commons Attribution 4.0 International License.

[Read Full License](#)

Version of Record: A version of this preprint was published at Nature Communications on April 25th, 2023. See the published version at <https://doi.org/10.1038/s41467-023-37905-y>.

Abstract

Background

Study of the geographic distribution of cellular populations and their interaction with malignant cells in non-small cell lung cancer (NSCLC) is essential to understand the roles of cellular populations and potentially design new therapeutic approaches.

Material and Methods

We studied 225 formalin-fixed, paraffin-embedded tumor tissue samples from patients with stage I-III NSCLC—142 adenocarcinomas and 83 squamous cell carcinomas—placed in tissue microarrays. Twenty-three markers were used, including T-cell, B-cell, immune checkpoint, and myeloid cell markers, placed in five multiplex immunofluorescence panels. We used dimensional data reduction and cellular spatial distribution to identify cell phenotypes and their cellular distribution across panels. In addition, we analyzed associations between cellular spatial distribution patterns and clinicopathologic variables, tumor mutational status, and outcomes.

Results

Overall, we observed two patterns of cellular distribution—unmixed and mixed—related to T-cells, B-cells, granulocytic cells, and macrophages, and we detected various cellular interactions between malignant and immunosuppressive cells and various associations between cell distribution and clinicopathologic characteristics. Cellular distribution patterns and the distance from various cell phenotypes to malignant cells were associated with recurrence-free survival and overall survival in univariate and multivariable analysis.

Conclusions

Diverse populations of tumor cells and tumor-associated immune cell phenotypes can be present in NSCLC samples. Spatial distribution is a new tool to better understand the tumor microenvironment and help select therapeutic interventions.

Introduction

Despite recent advances in chemotherapy and immunotherapy, lung cancer, particularly non-small cell lung cancer (NSCLC), remains one of the most commonly diagnosed malignancies and often has poor overall outcomes (1). Several analyses of NSCLC patients showed that adjuvant chemotherapy improved 5-year overall survival (OS) rates by only 5.4% (2). Another meta-analysis of 1,154 patients with stage II-III NSCLC showed that neoadjuvant chemotherapy with surgery was superior to surgery alone but had no

benefit compared with adjuvant chemotherapy (3). Moreover, the clinical effects of adjuvant tyrosine kinase inhibitors or anaplastic lymphoma kinase inhibitors in NSCLC remain limited (4). Antibodies targeting immune checkpoints (5) in NSCLC were recently shown to have a survival benefit (6, 7), improving 5-year OS rates in 20% of unselected patients and up to 40% of patients with high PD-L1 expression (8). However, despite these promising results, a substantial proportion of patients receiving these treatments exhibited disease progression (9).

Studying the interaction between malignant cells and tumor-associated immune cells (TAICs) using spatial distribution is essential to identify possible factors of tumor progression, relapse, or outcomes. This has been demonstrated not only in NSCLC (10) but also in other tumor types, such as breast cancer (11) and colon cancer (12). Malignant cells can utilize various pathways to avoid immune surveillance (13, 14), and identifying such mechanisms of progression can help identify potential new targeting strategies for lung cancer immunotherapy (15). The current study aimed to characterize the cellular composition of NSCLC and examine the spatial distribution of cell populations in NSCLC using multiplex immunofluorescence (mIF) panels. We also analyzed associations between cellular spatial distribution and clinicopathologic features and molecular profiles of NSCLC.

Materials And Methods

Tissue Specimens and Microarray

We examined specimens from 225 patients with stage I-III primary NSCLC, 142 of which were adenocarcinomas (ADCs) and 83 squamous cell carcinomas (SCCs). The patients had not received neoadjuvant therapy and were evaluated and underwent surgical resection at The University of Texas MD Anderson Cancer Center between 1997 and 2012. Tissue specimens were obtained from the Tissue Biospecimen and Pathology Resource, following informed consent under protocols approved by the Institutional Review Board. Tumors were classified using the 8th American Joint Committee on Cancer guidelines (16). Tissue microarray (TMA) sections were prepared using three 1.0-mm tissue cores obtained from the center, middle, and periphery of formalin-fixed and paraffin-embedded histologic sections. Clinical and pathologic information, including demographic data, age, sex, tobacco history, smoking status, tumor size, tumor stage, adjuvant treatment, and mutational tumor status (*KRAS* or *EGFR*), was collected from medical records. Follow-up information for recurrence-free survival (RFS) and OS rates were also retrieved from the patients' electronic medical records (**Supplementary Table 1**).

mIF Staining and Analysis

mIF staining was performed using methods similar to those previously described and validated (17). Briefly, formalin-fixed, paraffin-embedded TMA sections of 4- μ m thickness were stained using 5 panels containing the following antibodies: panel 1, cytokeratin (CK), CD3, CD8, PD-1, PD-L1, and CD68; panel 2, CK, CD3, CD8, CD45RO, granzyme B (GZB), and FOXP3; panel 3, CK, CD3, PD-L1, B7-H3, B7-H4, IDO-1, and VISTA; panel 4, CK, CD3, ICOS, LAG3, OX40, TIM3, and CD20; and panel 5, CK, Arg-1, CD11b, CD14, CD33, CD66b, and CD68. All markers were stained in sequence using their respective fluorophore contained in

the Opal 7 IHCKit (catalog #NEL797001KT; Akoya Biosciences, Waltham, MA) for the panels with 6 antibodies, and coumarin fluorophore was added in the panels with 7 antibodies (**Supplementary Table 2**). Positive (human reactive tonsils) and negative or autofluorescence controls (human reactive tonsils including the antibodies but without any fluorophores) were included in each run of staining (18). The stained slides were scanned using the multispectral microscope Vectra Polaris 3.0 imaging system (Akoya Biosciences) under fluorescence conditions at low magnification (10×), and then each core was viewed at high magnification (20×). Each core from the TMAs was analyzed using the InForm 2.4.0 digital image analysis software (Akoya Biosciences). Marker co-localization was used to identify the most relevant specific cell phenotypes from each mIF panel, as shown in **Supplementary Table 3**. Densities of each cell phenotype were quantified, and the final data were expressed as the number of cells/mm². The data were consolidated using R studio 3.5.3 (Phenopter 0.2.2 packet; Akoya Biosciences).

Immune Cell Phenotype Characterization

We created cord plots to better visualize cell phenotypes based on the co-expression of markers used in the 5 mIF panels. Additionally, dimensional reduction clustering was applied using uniform manifold approximation and projection (UMAP) to characterize all possible cell populations in each panel (19, 20). The results were plotted using R studio software v.3.6.1 and Python v. 3.8.9.

Spatial Cellular Distribution Analysis

To define spatial pattern distributions and cellular interactions between CK + malignant cells and TAICs, we compared the empirically derived cross G function curve with the theoretical Poisson curve (median distances of the specific cells from malignant cells between samples), obtained by assuming the same intensity pattern is observed in each sample, as described previously (17), to characterize patterns of cellular distribution and possible regulatory interactions between the cells. Furthermore, using the spatial point pattern distribution of the cell phenotypes relative to malignant cells, we measured the distance from CK + malignant cells to each cell phenotype included in the panels using a matrix created with each cell's X and Y coordinates in R studio software v.3.6.1. We applied the median nearest neighbor function from CK + malignant cells to CD3 + T-cells, CD20 + B-cells, CD68 + macrophages, and CD66b + granulocytic cells (PMNs), as well as to the other cell phenotypes, to determine where these TAICs were located; specifically, whether the TAICs were close to (equal to or less than the median distance) or far from (more than the median distance) the CK + malignant cells (19).

We expanded the characterization of patterns of cellular distribution and distances and combined these two results to identify four groups of cellular immunologic distribution:

Group 1. Mixed pattern with close median distances to the malignant cells

Group 2. Mixed pattern with long median distances to the malignant cells

Group 3. Unmixed pattern with close median distances to the malignant cells

Group 4. Unmixed pattern with long median distances to the malignant cells

Statistical Methods

For statistical analysis, densities and distances of various cell phenotypes from malignant cells were dichotomized: values greater than the median were considered high density or long distance and values equal to or lower than the median were considered low density or close distance. For patterns of cellular distribution, a score ranging from -10 to 10 in the comparison of G function curve with the theoretical Poisson curve indicated a mixed pattern and a score > 10 indicated an unmixed pattern, for various TAICs. Nonparametric tests were used to assess associations in the patterns of cellular distribution and spatial distance analysis from malignant cells to TAICs, and associations between cellular distribution patterns and clinicopathologic features were evaluated using the Wilcoxon rank-sum or Kruskal-Wallis test. Univariate analyses were based on the Kaplan-Meier method, and the log-rank test was used to determine whether patterns of cellular distribution, cellular distances, or cellular immunologic distribution groups were associated with RFS or OS. Cox proportional hazards models were used to evaluate associations between outcomes and the four immunologic cellular distribution groups, controlling for clinicopathologic characteristics. A *P* value of less than 0.05 was considered statistically significant. All analyses and data visualization were performed in R 3.6.0 and 3.6.1 (released April 2019; <https://www.r-project.org>), R studio 3.5.3 (Phenopter 0.2.2 packet; Akoya Biosciences), Python v.3.8.9, and/or GraphPad Prism v.9.0.0.

Results

We analyzed expression of 23 markers, including CK, CD3, CD8, CD68, GZB, CD45RO, FOXP3, PD-1, PD-L1, B7-H3, B7-H4, IDO-1, VISTA, ICOS, LAG3, OX40, TIM3, CD20, Arg-1, CD11b, CD14, CD66b, and CD33, placed in five mIF panels. We identified different cell phenotypes by marker co-expression, as shown in Fig. 1. Cord plot visualization helped to show the inter-relationships between markers and the co-expression of the markers together as well as by individual panel (Fig. 1, **Supplementary Fig. 1**). Dimension reduction plots and unsupervised cellular clustering identified diverse cell cluster populations based on marker co-expression in each mIF panel (Fig. 2).

Co-expression of Immune Checkpoint Molecules on Malignant Cells

Cord plots and UMAP plots showed that multiple immune checkpoints are expressed simultaneously by malignant cells. We found that PD-L1, B7-H3, B7-H4, and IDO-1 immune checkpoints were expressed by malignant cells, in various densities and combinations (Fig. 2, **Supplementary Fig. 1**). In addition, our dataset captured rare cell populations such as malignant cells expressing OX40; these populations were absent from previous studies and different from other cell phenotypes (Fig. 2) that would be expected to

escape from the phenotypes listed in **Supplementary Table 3**. Overall, the cellular densities of these checkpoint molecules were higher in malignant cells from SCC than in those from ADC. The most predominant immune checkpoint expressed in malignant cells from ADC and SCC was B7-H3 (median, 307.79 cells/mm²), followed by PD-L1 (median, 77.265 cells/mm²), OX40 (median 25.38 cells/mm²), B7-H4 (median, 19.17 cells/mm²), and IDO-1 (median, 7.08 cells/mm²), and significantly higher densities of B7-H3 and B7-H4 in were observed in SCC than in ADC ($P < 0.001$ for both immune checkpoints), whereas significantly higher densities of IDO-1 were observed in ADC than in SCC ($P = 0.015$; **Supplementary Table 4**). Additionally, the inter-relationships between markers through cord plots and UMAP clusters showed several other combinations of immune checkpoints (Fig. 2, **Supplementary Fig. 1**). This illustrates the heterogeneity of marker co-expression and clusters, suggesting that several pathways may be activated in the malignant cells as part of their escape from immune surveillance.

Characterization of T-Cell and B-Cell Populations

The most common T-cell and B-cell subpopulation densities are shown in **Supplementary Table 4** and **Supplementary Fig. 1**. Although we observed high amounts of classic T-cells and B-cells, such as CD3 + CD8 + cytotoxic T-cells (median, 136.51 cells/mm²), CD3 + CD45RO + memory T-cells (median, 57.39 cells/mm²), CD3 + CD8 + CD45RO + cytotoxic memory T-cells, (median, 25.44 cells/mm²), and CD20 + B-cells (median, 80.07 cells/mm²), we also observed substantial densities of suppressive T-cells such as CD3 + CD8^{neg}FOXP3 + regulatory T-cells (median, 24.10 cells/mm²), as well as T-cells and B-cells expressing other suppressive markers. We observed high densities of cells expressing PD-1 (median, 39.53 cells/mm²) and PD-L1 (median, 41.935 cells/mm²), as well as CD3 + LAG3+ (median, 229.81 cells/mm²), CD3 + ICOS+ (median, 36.19 cells/mm²), CD3 + OX40+ (median, 12.07 cells/mm²), CD3 + B7-H3+ (median, 8.86 cells/mm²), and CD3 + TIM3 + cells (median, 6.64 cells/mm²). We also observed high quantities of B-cells expressing ICOS (median, 7.44 cells/mm²), OX40 (median, 4.72 cells/mm²), and LAG3 (median, 31.10 cells/mm²). Checkpoints IDO-1 and VISTA in T-cells and TIM3 in B-cells were observed in low densities. Other T and B subcellular populations were identified and clustered using co-expression of the markers across panels, as shown in Fig. 2, illustrating the variability of T-cell and B-cell phenotypes in NSCLC, in particular with checkpoint inhibitors. We did not detect T-cells or B-cells expressing B7-H4. Compared with SCC, we observed significantly higher densities of CD3 + CD8 + cytotoxic T-cells, CD3 + CD45RO + memory T-cells, CD3 + CD8 + CD45RO + cytotoxic memory T-cells, CD3 + IDO-1 + T-cells, and CD3 + TIM3 + cells in ADC. In contrast, significantly higher densities of CD3 + PD-L1 + and CD3 + CD8 + PD-1 + PD-L1 + antigen-experienced PD-L1 cytotoxic T-cells were observed in SCC than in ADC (**Supplementary Table 4, Supplementary Fig. 1**).

Macrophages and Myeloid-Derived Suppressor Cell (MDSC) Phenotypes

Myeloid cell populations, including tumor-associated macrophages (TAMs), type II TAMs, and MDSCs, were detected. High densities of CD68 + TAMs (median, 318.32 cells/mm²), CD68 + CD11b + myeloid dendritic cells (median, 231.11 cells/mm²), CD66b + PMNs (median, 83.79 cells/mm²), CD66b + CD11b +

immature PMNs (median, 33.58 cells/mm²), and CD11b + CD66b + CD33 + granulocytic myeloid-derived suppressor cells (MDSC-PMNs; median, 11.44 cells/mm²) were observed in NSCLC, suggesting an important myeloid-suppressive component in these tumors. Other myeloid cells such as CD68 + Arg-1 + type II TAMs, CD68 + Arg-1 + CD11b + immature type II TAMs, and CD11b + Arg-1 + CD14 + CD33 + monocytic MDSCs were observed, but in low densities (**Supplementary Table 4**). Significantly higher densities of CD68 + CD11b + myeloid dendritic cells, as well as CD66b + PMNs and CD11b + CD66b + immature PMNs, were observed in SCC than in ADC (**Supplementary Fig. 1, Supplementary Table 4**).

Patterns of Cellular Distribution in the Tumor Microenvironment

After comparing the empirically derived G function curves from T-cells, B-cells, PMNs, and macrophages (as critical markers) with the theoretical Poisson function curve, we identified two patterns of distribution: mixed or heterogeneous (score ranging from - 10 to 10; Fig. 3A) and unmixed or clustering (score > 10; Fig. 3B), independent of histologic type (ADC or SCC). We found that 17 of 35 expected cell phenotypes had a mixed pattern and 17 had an unmixed pattern, in both ADC and SCC, Table 1. Furthermore, only CD3 + CD45RO + FOXP3 + memory regulatory T-cells showed significantly different patterns between ADC and SCC (i.e., mixed pattern in ADC and unmixed in SCC; Table 1). In both histologic types, most of the cell phenotypes showing an unmixed pattern were immunosuppressive, including T-cells, B-cells, and macrophages expressing immune checkpoint markers and MDSC phenotypes. In addition, we identified two groups of cell phenotypes using this approach: cells in direct contact with malignant cells (suppressive T-cells and MDSC-PMNs) showing a mixed pattern, and cells with less contact with malignant cells (including macrophages, suppressor macrophages, cytotoxic T-cells, and memory T-cells; Fig. 3C) showing an unmixed pattern, suggesting that the tumor microenvironment in most cases is immunosuppressive.

Table 1. Patterns of cellular distribution according to histologic type.

Panel	Phenotype	Pattern of malignant cells*			Pt
		NSCLC	Adenocarcinoma	Squamous cell carcinoma	
1	CD3+	27.96	25.05	38.86	0.942
	CD3+CD8+	25.81	24.03	31.92	0.902
	CD3+PD-1+	16.53	12.17	23.92	0.132
	CD3+PD-L1+	20.19	19.45	22.64	0.386
	CD3+CD8+PD-1	3.20	2.89	4.79	0.996
	CD3+CD8+PD-L1+	11.07	10.82	13.02	0.769
	CD3+PD-1+PD-L1+	5.87	5.65	7.59	0.504
	CD3+CD8+PD-1+PD-L1+	2.18	2.05	2.19	0.631
	CD68+	17.50	15.55	21.86	0.334
	CD68+PD-L1+	9.33	8.10	9.81	0.889
	2	CD3+	27.30	22.98	37.84
CD3+CD8+		29.88	27.20	37.36	0.644
CD3+CD8+GZB+		0.36	-0.04	0.89	0.372
CD3+CD45RO+		35.84	30.14	48.40	0.933
CD3+CD8+CD45RO+		31.10	25.35	41.40	0.294
CD3+CD8 ^{neg} FOXP3+		29.55	26.75	37.41	0.428
CD3+CD45RO+FOXP3+		24.30	8.92	14.80	<0.001
3	CD3+	29.14	28.38	32.00	0.260
	CD3+B7-H3+	26.49	25.31	28.83	0.816
	CD3+B7-H4+	7.01	5.37	14.39	0.010
	CD3+IDO-1+	28.04	26.57	30.28	0.837
	CD3+PD-L1+	30.27	28.75	32.32	0.230
	CD3+VISTA+	17.22	15.04	21.16	0.274
4	CD3+	21.00	20.33	28.00	0.633
	CD3+ICOS+	12.00	11.59	14.00	0.647
	CD3+LAG3+	22.30	19.03	29.50	0.633
	CD3+OX40+	6.35	4.84	9.50	0.232

	CD3+TIM3+	4.07	5.22	3.00	0.261
	CD20+	6.05	4.14	9.00	0.314
	CD20+ICOS+	4.11	2.15	7.00	0.342
	CD20+OX40+	3.00	2.82	3.50	0.954
	CD20+TIM3+	1.72	1.91	1.00	0.797
	CD20+LAG3+	10.89	8.95	15.50	0.280
5	CD68+	19.64	17.31	24.76	0.884
	CD68+Arg-1+	1.20	0.61	2.00	0.740
	CD68+Arg-1+CD11b+	1.07	0.45	2.00	0.893
	CD68+CD11b+	21.84	18.95	26.81	0.365
	CD66b+	3.54	2.13	6.32	0.186
	CD11b+CD66b+	4.00	2.54	8.50	0.720
	CD11b+Arg-1+CD14+CD33+	1.19	1.11	1.58	0.780
	CD11b+CD66b+CD33+	3.00	1.96	6.00	0.113

Note: NSCLC, non-small cell lung cancer.

*A score of -10 to 10 indicates a mixed pattern, and a score >10 indicates an unmixed pattern.

†*P* values indicate comparison between adenocarcinoma and squamous cell carcinoma.

Cellular Spatial Distances of TAI-Cs from Malignant Cells in the Tumor Microenvironment

Using the median nearest neighbor distance from malignant cells to various primary TAI-Cs, we observed that in NSCLC, the median distance from malignant cells to CD3 + T-cells was 36.46 μm ; to CD20 + B-cells, 104.61 μm ; to CD68 + macrophages, 42.24 μm ; and to CD66b + PMNs, 87.24 μm (Table 2). We characterized the subfamilies inside these median radii as close to malignant cells and those outside these median radii as far from malignant cells. Using this dichotomy, we observed the proximity of T-cells expressing inhibitory checkpoint markers, such as PD-L1, B7-H3, IDO-1, and LAG3, from malignant cells expressing checkpoint inhibitors PD-L1, B7-H3, B7-H4, IDO-1, and OX40 (**Supplementary Table 5**). CD3 + CD8 + PD-1 + PD-L1 + antigen-experienced PD-L1 cytotoxic T-cells were located closer to the CK + PD-L1^{neg} malignant cells (median, 19.41 μm) than to CK + PD-L1 + malignant cells (median, 39.22 μm). Similarly, CD3 + PD-L1 + cells were observed next to B7-H4 + malignant cells (median, 26.67 μm) and IDO-1 +

malignant cells (median, 24.07 μm). Although the median distance of CD68 + macrophages from malignant cells was 42.24 μm , CD68 + macrophages and PD-L1 + macrophages were closer to PD-L1^{neg} malignant cells (median, 12.90 μm and 51.89 μm , respectively) than to PD-L1 + malignant cells (median, 42.31 μm and 119.71 μm , respectively), suggesting that inhibitory signals are closer to PD-L1^{neg} malignant cells than to PD-L1 + malignant cells.

Table 2. Median distances from malignant cells for various cell phenotypes according to histologic type.

Panel	Phenotype	Median distance from malignant cells, μm			<i>P</i> *
		NSCLC	Adenocarcinoma	Squamous cell carcinoma	
1	CD3+	29.28	38.38	26.88	0.002
	CD3+CD8+	68.99	58.62	61.36	0.003
	CD3+PD-1+	104.31	113.53	99.03	0.181
	CD3+PD-L1+	105.56	105.02	105.56	0.870
	CD3+CD8+PD-1	220.89	245.71	203.72	0.163
	CD3+CD8+PD-L1+	218.69	218.69	216.45	0.551
	CD3+PD-1+PD-L1+	292.43	287.91	297.80	0.544
	CD3+CD8+PD-1+PD-L1+	350.48	337.23	367.32	0.389
	CD68+	42.01	44.52	37.57	0.168
	CD68+PD-L1+	113.40	111.04	113.41	0.778
2	CD3+	30.42	27.66	42.28	<0.001
	CD3+CD8+	60.40	54.07	78.40	<0.001
	CD3+CD8+GZB+	240.62	243.26	238.91	0.576
	CD3+CD45RO+	91.15	75.96	125.49	<0.001
	CD3+CD8+CD45RO+	140.69	114.36	186.28	0.001
	CD3+CD8 ^{neg} FOXP3+	135.08	121.99	147.59	0.002
	CD3+CD45RO+FOXP3+	252.20	221.84	281.49	0.013
3	CD3+	28.44	48.79	22.55	<0.001
	CD3+B7-H3+	57.52	191.96	48.42	0.154
	CD3+B7-H4+	173.56	382.67	173.56	0.052
	CD3+IDO-1+	43.59	374.84	38.70	0.002
	CD3+PD-L1+	125.09	135.49	115.57	0.203
	CD3+VISTA+	121.13	268.33	94.88	0.023
4	CD3+	36.46	43.22	29.56	0.023
	CD3+ICOS+	105.15	113.21	102.80	0.362
	CD3+LAG3+	46.46	53.22	39.56	0.023
	CD3+OX40+	201.04	233.01	184.20	0.019

	CD3+TIM3+	256.75	295.88	230.01	0.007
	CD20+	104.61	118.82	91.79	0.060
	CD20+ICOS+	257.72	277.59	232.22	0.084
	CD20+OX40+	305.35	353.03	266.19	0.041
	CD20+TIM3+	448.24	453.10	444.30	0.436
	CD20+LAG3+	158.94	204.55	147.82	0.017
5	CD68+	42.24	43.05	40.60	0.513
	CD68+Arg-1+	367.65	323.11	412.70	0.007
	CD68+Arg-1+CD11b+	380.65	324.53	412.70	0.020
	CD68+CD11b+	51.81	51.13	52.30	0.613
	CD66b+	87.24	87.98	85.22	0.385
	CD11b+CD66b+	133.49	121.79	141.08	0.358
	CD11b+CD66b+CD33+	214.99	199.89	217.28	0.864
	CD11b+Arg-1+CD14+CD33+	433.09	428.94	446.70	0.956

Note: NSCLC, non-small cell lung cancer.

**P* values indicate comparison between adenocarcinoma and squamous cell carcinoma.

Additionally, upon examining the radii from malignant cells to other distinct TAIC phenotypes, we observed that CD3 + CD8 + cytotoxic T-cell, CD3 + CD45RO + memory T-cell, CD3 + CD8^{neg}FOXP3 + regulatory T-cell, B-cell, and myeloid cell subpopulations were located far from the malignant cells, as shown in the heat maps in Fig. 3D-H. CD3 + CD8 + cytotoxic T-cells were close to CD3 + CD8^{neg}FOXP3 + regulatory T-cells (median, 26.73 μ m), CD3 + CD45RO + memory T-cells (median, 40.83 μ m), and CD3 + CD8 + CD45RO + cytotoxic memory T-cells (median, 43.05 μ m), suggesting a possible inhibitory action from this T-cell phenotype to cytotoxic and memory T-cells (**Supplementary Table 4**). Furthermore, we observed that cytotoxic T-cells, memory T-cells, cytotoxic memory T-cells, regulatory T-cells, and effector memory T-cells were significantly closer to malignant cells in ADC than in SCC. In contrast, a considerably closer distance from malignant cells to T-cells expressing IDO-1, VISTA, LAG3, OX40, and TIM3 and B-cells expressing OX40 and LAG3 was observed in SCC compared with ADC. Closer distances between type II macrophages and monocytic MDSCs were detected in SCC than in ADC (Table 2), suggesting that SCC has more suppressive cell phenotypes relatively close to malignant cells than does ADC.

Cellular Immunologic Distribution Landscape

By combining the cellular distribution patterns with the median distances of TAICs from malignant cells, we identified four cellular immunologic distribution groups for each cell phenotype across the panels:

Group 1. Mixed pattern with close median distances to the malignant cells

Group 2. Mixed pattern with long median distances to the malignant cells

Group 3. Unmixed pattern with close median distances to the malignant cells

Group 4. Unmixed pattern with long median distances to the malignant cells

[⚠️Au: this sentence is repeated above] Supplementary Table 6 shows the cellular immunologic distribution of the main cell populations, CD3 + T-cells, CD20 + B-cells, CD68 + macrophages, and CD66b + PMNs.

The predominant cellular immunologic distribution for CD3 + T-cells was group 2 (mixed pattern with long median distances to malignant cells), which was observed in 31.6% of ADC specimens, followed by group 4 (unmixed pattern with long median distances to the malignant cells), which was observed in 24.9% of SCC specimens. CD20 + B-cells did not show any predominant cellular immunologic distribution in either ADC or SCC. For CD68 + macrophages, group 2 and 4 were the predominant cellular immunologic distribution in ADC (18.6% of specimens), followed by group 2 (16.9% of specimens). The dominant cellular immunologic distribution of CD68 + macrophages in SCC was group 3 (13.6% of specimens), followed by group 2 (11.0% of specimens). For CD66b + PMNs, group 1 (mixed pattern with close median distances to the malignant cells) was the predominant cellular immunologic distribution (24.0% of ADC samples), followed by group 3 (unmixed pattern with close median distances to malignant cells, 20.8% of ADC samples). In contrast, in SCC, the predominant cellular immunologic distribution for CD66b + PMNs was group 3 (16.9% of samples), followed by group 2 (11.0% of samples).

Association of Cellular Distribution Patterns and Spatial Metrics of TAICs with Clinical Variables

To study associations between clinical variables and cellular patterns of distribution and spatial cellular distances from malignant cells, we used the comparison of the G function curve with the theoretical Poisson curve and the median distance from malignant cells to various cell phenotypes.

Using the cellular patterns of distribution, in ADC specimens from patients who were smokers, a mixed pattern of CD3 + T-cells was observed compared with specimens from patients who were nonsmokers. In contrast, an unmixed pattern of CD3 + CD8 + CD45RO + cytotoxic memory T-cells was observed in specimens from smokers compared with nonsmokers (Fig. 4A). Compared with smaller tumors (≤ 3.15 cm; the median within the group was used as a cutoff for tumor size comparisons), ADC tumors > 3.15 cm showed a mixed pattern of CD3 + PD-L1 + cells (Fig. 4B). ADC *KRAS*-mutant tumors showed a mixed pattern of CD68 + PD-L1 + cells compared with wild-type tumors (Fig. 4C). In SCC, tumors > 3.8 cm showed an unmixed pattern of CD11b + CD66b + CD33 + MDSC-PMNs compared with tumors ≤ 3.8 cm

(Fig. 4D). Also in SCC, patients who received adjuvant therapy after surgery had tumors with a predominantly unmixed pattern of CD3 + PD-1 + PD-L1+, CD3 + ICOS+, and CD11b + CD66b + CD33 + cells compared with those from patients who did not receive adjuvant therapy after treatment (Fig. 4E).

In ADC specimens from smokers, we observed a close median distance from malignant cells to suppressive TAIC phenotypes such as PD-L1 + T-cells, CD3 + CD8 + PD-L1 + cytotoxic T-cells, type II macrophages, and MDSC-PMNs. ICOS + B-cells were close to malignant cells. In ADC specimens from nonsmokers, malignant cells were located close to CD3 + CD8^{neg}FOXP3 + regulatory T-cells, CD3 + CD8 + cytotoxic T-cells, and CD3 + CD45RO + memory T-cells (Fig. 5A).

Among ADC specimens, tumors ≤ 3.15 cm showed CD3 + CD8 + cytotoxic T-cells, CD3 + CD8 + CD45RO + FOXP3 + cytotoxic memory T-cells, CD3 + CD8^{neg}FOXP3 + regulatory T-cells, CD3 + CD45RO + memory regulatory T-cells, IDO-1 + T-cells, B-cells, and LAG3 + B-cells located closer to malignant cells than in the larger tumors (Fig. 5B). In SCC, tumors larger than the median (> 3.8 cm) showed closer distances from malignant cells to macrophages and IDO-1 + T-cells than did smaller tumors (Fig. 5G). In ADC specimens from patients who received adjuvant therapy after surgery, we observed closer proximity from malignant cells to CD3 + CD8 + PD-1 + PD-L1 + cytotoxic T-cells and to PD-L1 + macrophages than in specimens from patients who did not receive adjuvant therapy (Fig. 5C).

Close distances from malignant cells to TIM3 + B-cells were observed in stage II ADC specimens. Likewise, close distances from cytotoxic CD3 + CD8 + T-cells to PD-L1 + macrophages were observed in stage II and III specimens. Moreover, close distances from cytotoxic CD3 + CD8 + T-cells to CD3 + CD8^{neg}FOXP3 + regulatory T-cells were observed in stage I and II specimens (Fig. 5D).

EGFR-mutant tumors had closer distances from malignant cells to CD3 + PD-1 + PD-L1 + T-cells and from CD3 + CD8 + activated cytotoxic T-cells to CD3 + CD8^{neg}FOXP3 + regulatory T-cells than did wild-type tumors in ADC. In addition, *KRAS*-mutant tumors had closer distances from malignant cells to MDSC-PMNs than did wild-type tumors (Fig. 5E, F).

Associations between Cellular Patterns and Distances and Patient Outcomes

We next examined whether cellular distribution patterns of TAICs or TAIC distances to malignant cells were associated with patient outcomes. Univariate analysis of cellular distribution patterns (Fig. 6A) showed that the unmixed pattern of CD11b + Arg-1 + CD14 + CD33 + MDSC-PMNs was associated with poorer RFS than the mixed pattern in ADC (**Supplementary Fig. 2A**). Also in ADC, we observed that the mixed pattern of CD20 + TIM3 + B-cells was associated with worse OS than the unmixed pattern of this B-cell phenotype (Fig. 6B). In contrast, unmixed patterns in CD66b + PMNs and CD11b + Arg-1 + CD14 +

CD33 + MDSC-PMNs were associated with worse OS than mixed patterns in ADC (Fig. 6C, D). In SCC, the mixed pattern in CD3 + PD-L1 + T-cells and CD3 + CD8 + GZB + activated cytotoxic T-cells was associated with better RFS than the unmixed pattern (**Supplementary Fig. 1B, C**). However, the mixed pattern in CD3 + VISTA + T-cells was associated with poorer OS than the unmixed pattern for this cell phenotype (Fig. 6E).

Using distances from malignant cells to TAICs (Fig. 6F), univariate analysis in our cohort showed that long distances from malignant cells to CD66b + PMNs and to CD11b + Arg-1 + CD14 + CD33 + MDSC-PMNs in ADC were associated with better RFS than were close distances (**Supplementary Fig. 2D, E**). In SCC, long distances from malignant cells to CD3 + PD-L1 + T-cells and close distances from malignant cells to CD3 + ICOS + T-cells were associated with better RFS (**Supplementary Fig. 2F, G**). Furthermore, close distances from malignant cells to CD3 + CD8 + cytotoxic T-cells, CD3 + CD8 + GZB + activated cytotoxic T-cells, and CD68 + macrophages were associated with better OS than long distances in ADC (Fig. 6G-I). In contrast, close distances from malignant cells to CD3 + B7-H3 + T-cells were associated with worse OS than long distances (Fig. 6J).

Next, we studied the effects of the four groups of cellular immunologic distribution, combining cellular patterns of TAIC distribution with TAIC distances from malignant cells, on patient outcomes (**Supplementary Fig. 3**). Univariate analysis of these four groups showed that the mixed pattern of CD3 + T-cells with close or long distances to malignant cells and the unmixed pattern with close distances (groups 1, 2, and 3) were associated with better RFS than the unmixed pattern with long distances to malignant cells in ADC (group 4; **Supplementary Fig. 3A**). In SCC, an unmixed pattern of CD3 + PD-L1 + cells with close distances to malignant cells was associated with better RFS compared with the other three groups of cellular immunologic distribution (**Supplementary Fig. 3B**). In addition, the mixed pattern of CD3 + ICOS + cells with close distances to malignant cells (group 1), as well as the mixed pattern with long distances and unmixed pattern with close distances (groups 2 and 3), was associated with better RFS compared with the unmixed pattern with long distances (group 4) in ADC. We also found that a mixed pattern of CD3 + T-cells with close distances to malignant cells (group 1) was associated with better OS compared with the other immunologic distribution groups, especially the unmixed pattern with long distances to malignant cells (group 4), in ADC. However, for CD68 + macrophages, groups 2 and 3 were associated with better OS compared with group 4 in ADC.

Finally, we analyzed the four cellular immunologic distribution groups in a Cox proportional hazards regression model adjusted for histologic type, smoking status, tumor size, *KRAS* mutation status, and *EGFR* mutation status. As shown in **Supplementary Table 7**, patients with a mixed pattern of CD3 + IDO-1 + T-cells with close distances to malignant cells (group 1) had worse OS than those with the group 4 cellular immunologic distribution. Factors associated with better OS included wild-type *EGFR*, mixed pattern of CD3 + CD45RO + memory T-cells with close distances to malignant cells, and mixed pattern of CD68 + macrophages with long distances to malignant cells.

Discussion

In the current study, we analyzed a TMA set containing tumor specimens obtained from a large cohort of patients with stage I-III NSCLC using 23 markers, including T-cell, B-cell, immune checkpoint, and myeloid cell markers, placed in 5 mIF panels. Cord plots and UMAP clusters based on marker co-expression were used to visualize different TAIC phenotypes across different panels. In addition, we identified rare cell types, showing the diversity of cell populations in NSCLC. Immune checkpoints expressed by malignant cells were observed in several combinations within specimens, as well as in TAICs across specimens. Overall, we observed two patterns of cellular distribution—mixed and unmixed—related to T-cells, B-cells, macrophages, and PMNs as the main cell phenotypes. Cellular patterns of distribution, as well as the distance between malignant cells and various cell phenotypes, showed different associations with clinicopathologic characteristics, including smoking status, tumor size, final tumor stage, adjuvant therapy, and mutational status. Kaplan-Meier survival curves showed that patterns and distances from malignant cells to different cell phenotypes were also associated with OS and RFS. Finally, we identified four groups of cellular immunologic patterns, which were also associated with OS and RFS in univariate analysis and Cox proportional hazards regression models.

We found that malignant cells expressing B7-H3 were most commonly observed in NSCLC, followed by malignant cells expressing PD-L1, OX40, B7-H4, and IDO-1. These checkpoints have adverse regulatory functions over T lymphocytes (21–24). Other immune checkpoints observed in our cohort, such as OX40 and ICOS, have co-stimulatory signals for T-cell activation in normal and pathologic conditions (25–27). Cord plots and UMAP plots showed that various TAICs and malignant cells could express these checkpoints. Although it was thought for a long time that OX40 expression was restricted to activated conventional T-cells, other TAICs, including malignant cells, have since been shown to express this marker (28). Overall, we observed higher densities of immune checkpoint markers in SCC than in ADC, particularly PD-L1, B7-H3, and B7-H4, showing that these immune checkpoints are predominantly expressed in solid tumors (29), creating a more immunosuppressive microenvironment. It is clear that in NSCLC, these immune checkpoint pathways are expressed simultaneously and are an essential mechanism of immune resistance against T-cell response (30, 31). Our findings confirm that malignant cells could express more than one checkpoint marker simultaneously, indicating that lung tumors can use more than one pathway to avoid the immune system (32, 33). Immune checkpoints are essential regulators of the immune system, initiating a productive immune response, preventing the onset of autoimmunity, or using tumors to avoid the immune system (34). In agreement with other studies (31), our results show that TAICs and malignant cells essentially drive these suppressive pathways. This knowledge of simultaneous co-expression can guide the study of rational combinations of agents for potential new therapeutic approaches.

Although we observed overall increased amounts of CD3 + CD8 + cytotoxic T-cells, CD3 + CD45RO + memory T-cells, CD3 + CD8 + CD45RO + cytotoxic memory T-cells, and CD20 + B-cells in the NSCLC specimens, we also detected a number of TAICs expressing co-inhibitory and co-stimulatory signatures, including PD-1, LAG3, TIM3, FOXP3, ICOS, and OX40, in higher amounts in SCC than in ADC. Similarly, we

observed that CD68 + macrophages, CD68 + CD11b + myeloid dendritic cells, and CD66b + PMNs were more predominant in SCC than in ADC. These observations suggest that various immunosuppressive cells are present in these tumors, possibly reflecting their relation to other factors such as smoking status or chronic obstructive pulmonary disease, increasing these cell populations as described previously (35). Although myeloid cell phenotypes such as CD68 + Arg-1 + type II macrophages, CD68 + Arg-1 + CD11b + type II immature tumor-associated macrophages, CD66b + CD11b + immature PMNs, Arg-1 + CD33 + CD14 + CD11b + monocytic MDSCs, and CD33 + CD66b + CD11b + MDSC-PMNs were observed in low densities, these were also present, playing their immunosuppressive roles (36).

By mapping the spatial organization of the TAICs as previously described (17), we observed mixed and unmixed cellular distribution patterns. Likely related to the dysfunctional signature observed in melanoma tumor tissues (37), we observed two groups of cells in relation to malignant cells: an immunosuppressive group, which has a mixed pattern indicating close interaction with malignant cells, and an immunoprotective group, which has an unmixed pattern with apparently less interaction with malignant cells. This immunoprotective group included CD3 + CD8 + cytotoxic T-cells, CD3 + CD8 + CD45RO + cytotoxic memory T-cells, CD3 + CD45RO + memory T-cells, and CD68 + macrophages.

Analysis of nearest neighbor median distance from malignant cells to CD3 + T-cells and macrophages showed that CD68 + cells are closer to malignant cells than are CD20 + B-cells and CD66b + PMNs. Although CD3 + CD8 + cytotoxic T-cells were among the most abundant cells in both ADC and SCC specimens, not many of these were close to malignant cells. In contrast, T-cells expressing PD-L1, B7-H3, B7-H4, IDO-1, and OX40 were located close to the malignant cells, suggesting that the distances from malignant cells and pattern of distribution, rather than the density of these cells, plays a critical role in cancer. Interestingly, CD3 + CD45RO + memory T-cells, CD3 + CD8^{neg}FOXP3 + regulatory T-cells, B-cells, and most myeloid cells were located far from malignant cells. However, CD3 + CD8^{neg}FOXP3 + regulatory T-cells play a solid immunosuppressive role in the tumor environment by releasing inhibitory cytokines (38), facilitating the action of other cell inhibitors. Cellular distribution patterns and cellular distances are not frequently studied and are not very well understood, but these patterns can give us essential information about tumor tissue biological processes related to different tumor characteristics (39).

The association of cellular distribution patterns with clinicopathologic features has not been previously described, and we believe that this information can help us better understand the biological behavior of tumors. For example, we observed that ADC specimens from smokers overall had a mixed pattern of distribution of CD3 + T cells and an unmixed pattern of CD3 + CD8 + CD45RO + effector memory T-cells. The largest ADC tumors showed an unmixed pattern of CD3 + PD-L1 + cells. In ADC *KRAS*-mutant tumors, we observed a mixed pattern of CD68 + PD-L1 + cells. In SCC, we observed changes in cellular distribution patterns predominantly in MDSC populations, which showed a mixed pattern of CD11b + CD66b + CD33 + cells in smaller tumors. Patients who received adjuvant therapy also had tumors with an unmixed pattern of malignant cells, with several T-cell inhibitory proteins and MDSC populations. ADC specimens from smokers also showed a close median distance from malignant cells to PD-L1 + T-cells, CD3 + CD8 + PD-L1 + cytotoxic T-cells, M2 macrophages, and MDSC-PMNs. This can be interpreted as tobacco's

immunosuppressive effect on the tumor microenvironment (35). In contrast, ADC specimens from nonsmokers showed close median distances from malignant cells to CD3 + CD8^{neg}FOXP3 + regulatory T-cells and, most importantly, from CD3 + CD8 + cytotoxic T-cells and CD3 + CD45RO + memory T-cells to CD3 + CD8^{neg}FOXP3 + regulatory T-cells, suggesting a different mechanism of inhibition than that observed in tumors from smokers.

Small tumors in ADC showed closer proximity from malignant cells to CD3 + CD8 + cytotoxic T-cells, CD3 + CD8 + CD45RO + cytotoxic memory T-cells, CD3 + CD8^{neg}FOXP3 + regulatory T-cells, CD3 + CD45RO + FOXP3 + memory regulatory T-cells, IDO-1 + T-cells, IDO-1 + B-cells, and LAG3 + B-cells compared with the larger tumors, suggesting that small tumors are more enriched in inhibitory signals. In SCC, large tumors showed closer distances from malignant cells to CD68 + macrophages and IDO-1 + T-cells than did small tumors. Furthermore, in ADC, stage II tumors showed closer proximity from malignant cells to TIM3 + B-cells than did stage III tumors, and stage I tumors showed closer proximity from cytotoxic T-cells to PD-L1 + macrophages and regulatory T-cells than did stage II tumors, suggesting changes according to the stage of the tumor. In tumors from patients who received adjuvant therapy after surgery, we observed closer distances from malignant cells to PD-1 + PD-L1 + cytotoxic T-cells and PD-L1 + macrophages than in tumors from patients who did not receive adjuvant therapy. This finding indicates that these markers could aid in the decision to administer adjuvant therapy, together with the current recommendations (40).

We found that distribution patterns and distances from malignant cells to different cell phenotypes could be associated with outcomes. Limited penetration among malignant cells, indicated by an unmixed pattern of distribution of MDSC-PMNs, was associated with poor RFS, and an unmixed pattern of CD66b + PMNs and MDSC-PMNs was associated with poor OS in ADC. These findings suggest that these cell phenotypes are acting as a barrier, limiting the actions of other activated T-cells. MDSCs are known to suppress T-cell activation and toxicity using various mechanisms (41). Although TIM3 has been reported in several T-cell populations, as well as dendritic cells and monocytes (42), we observed that a subset of CD20 + B-cells co-expressed coinhibitory molecules such as TIM3, and a mixed pattern of distribution was associated with poor OS. The action of TIM3 and other inhibitor molecules on this type of cell is unknown, and further investigation will be needed to understand the implications of these co-expression patterns. A mixed pattern of CD3 + CD8 + GZB + activated cytotoxic T-cells was associated with better RFS, suggesting that the interaction of these cells with malignant cells could prevent tumor recurrence in SCC. In contrast, a mixed pattern of CD3 + VISTA + T-cells was associated with poor OS, showing that the distribution of these cells next to malignant cells increases their immunosuppressive action. VISTA has a potential immunosuppressive influence on the tumor microenvironment for several types of T-cells in various cancers, including NSCLC, and immunotherapy targeting this protein is currently under investigation (43).

It is known that most, if not all, malignancies trigger an innate inflammatory response that builds up a pro-tumorigenic microenvironment that can resist treatment (44). This suggests that the close proximity of immunosuppressive cells to malignant cells and increased interactions between these cells in NSCLC, as we observed in the current study, enable tumors to avoid the immune system. In ADC, we also

observed that *EGFR*-mutant tumors had a significantly closer median distance from malignant cells to PD-1 + PD-L1 + T-cells and from CD3 + CD8 + GZB + activated cytotoxic T-cells to CD3 + CD8^{neg}FOXP3 + regulatory T-cells than did wild-type tumors. Compared with wild-type tumors, *KRAS*-mutant tumors showed closer distances from malignant cells to MDSC-PMNs, suggesting that mutational status affects cellular distribution.

Kaplan-Meier curves showed that in ADC, close distances from malignant cells to PMNs and MDSC-PMNs are associated with worse RFS than long distances. In SCC, close distances from malignant cells to PD-L1 + T-cells and long distances to ICOS + T-cells were associated with worse RFS. Our data also showed that close proximity of malignant cells to CD3 + CD8 + cytotoxic T-cells, CD3 + CD8 + GZB + activated cytotoxic T-cells, and macrophages was associated with better OS than long distances in ADC, suggesting that the cell-to-cell proximity of these cells mitigates the suppressive effect of inhibitory cells and supporting the findings of Barua et al (45). We also found that close distance from malignant cells to B7-H3 + T-cells was associated with worse OS. This suggests that the cellular spatial distribution of specific cell phenotypes is an independent factor associated with poor or better prognosis and can be used to select combinations of therapeutic strategies and determine patient prognosis (39), not only in NSCLC but also in other cancers (12).

Finally, by combining patterns of cellular distribution with cellular distances, we identified four groups of cellular immunologic patterns. In univariate analysis, we found that an unmixed pattern of CD3 + T-cells with long distances from malignant cells was associated with poor OS and RFS in ADC, and an unmixed pattern of CD68 + with long distances from malignant cells was associated with poor OS. An unmixed pattern of CD3 + PD-L1 + cells with close distances from malignant cells and a mixed pattern of CD3 + ICOS + cells with close distances from malignant cells were associated with better RFS. ICOS is known to have a dual role; co-stimulation confers an anticancer response, but ICOS signaling also engages regulatory T-cell activity induction (46), suggesting that the location and distribution of ICOS + cells can influence the activation of one of its roles. Furthermore, in multivariable analysis, a mixed pattern of CD3 + IDO-1 + cells with close distances to malignant cells was identified as an independent marker associated with poor OS, suggesting that location and distance of IDO1 + cells from malignant cells can drive an immunosuppressive microenvironment, which may be responsible for the resulting poor prognosis. IDO expression has been detected in various TAIC populations and has been shown to be related to lung cancer progression (47). In contrast, wild-type *EGFR*, a mixed pattern of CD3 + CD45RO + memory T-cells with close distances to malignant cells, and a mixed pattern of CD68 + macrophages with long distances to malignant cells were associated with better OS in multivariable analysis, suggesting that not only cellular patterns of distribution but also distance from malignant cells can influence outcomes. These findings highlight the importance of better understanding the complex relationships between malignant cells and immune cells in terms of their spatial distribution to direct the study of new therapeutic approaches.

The current study has some limitations. First, although our NSCLC specimens were collected retrospectively, which allowed us a large enough sample to examine varying cell phenotypes, those

phenotypes were displaced in different independent mIF panels, which limited the integration of the different cell phenotypes. Second, most of the patients from our cohort were smokers, which can influence the analysis between nonsmokers and smokers. Lastly, our specimens were placed in TMA format, which may induce under- or overrepresentation of the marker levels and spatial distribution owing to tumor heterogeneity.

In summary, our data showed that tumor cells and TAICs could produce multiple inhibitory factors in NSCLC. In studying the spatial distribution of various cellular populations, we could identify other associations between these cells and clinicopathologic variables in surgically resected ADC and SCC specimens. In addition, we identified several associations between specific cellular patterns of distribution and their distances that can negatively or positively influence patient outcomes; however, validation of our findings using a similar cohort of patients is needed.

Declarations

Acknowledgements

The Multiplex Immunofluorescence and Image Analysis Laboratory in the Department of Translational Molecular Pathology thanks its members, who contribute daily to quality multiplex immunofluorescence. We thank the pathology team in the Department of Translational Molecular Pathology for the image analysis and Grady Carson and Jose de Jesus Martinez for their advice during the spatial analysis. Editorial support was provided by Erica Goodoff from the Research Medical Library at The University of Texas MD Anderson Cancer Center.

Financial Support: This study was supported in part by the Multiplex Immunofluorescence and Image Analysis Laboratory in the Department of Translational Molecular Pathology. Financial support for the Cancer Immune Monitoring and Analysis Centers and Cancer Immunologic Data Commons Network was provided through the National Cancer Institute Cooperative Agreement U24CA224285 of The University of Texas MD Anderson Cancer Center Cancer Immune Monitoring and Analysis Centers. Financial support was also provided by the Cancer Prevention Research Institute of Texas Multi-Investigator Research Award (RP160668), The University of Texas Lung Specialized Programs of Research Excellence grant (P50CA70907), and MD Anderson's Institutional Tissue Bank Award through the Cancer Center Support Grant (P30CA016672) from the National Cancer Institute.

Competing Interests: The authors have no competing interests to declare.

Author Contributions: E.R.P. conceived the project, designed the analyses, interpreted the data, and wrote the manuscript; J.Z. designed the statistical plan and performed the statistical analyses; M.J. and A.T.

performed the tumor immune marker staining and scanning and participated in writing the manuscript; R.K.P. participated in the cellular spatial analysis; C.B. collected the clinical data; J.V.H. reviewed the manuscript; C.M. helped to collect the tumor specimens; J.L. participated in supervising the statistical analysis and interpretation; D.G. reviewed the manuscript; and I.I.W. participated in reviewing the manuscript. All authors reviewed the manuscript at all stages.

References

1. Zappa C, Mousa SA. Non-small cell lung cancer: current treatment and future advances. *Transl Lung Cancer Res.* 2016;5(3):288–300.
2. Pirker R. Adjuvant chemotherapy in patients with completely resected non-small cell lung cancer. *Transl Lung Cancer Res.* 2014;3(5):305–10.
3. MacLean M, Luo X, Wang S, Kernstine K, Gerber DE, Xie Y. Outcomes of neoadjuvant and adjuvant chemotherapy in stage 2 and 3 non-small cell lung cancer: an analysis of the National Cancer Database. *Oncotarget.* 2018;9(36):24470–9.
4. Wang L, Wang W. Safety and efficacy of anaplastic lymphoma kinase tyrosine kinase inhibitors in nonsmall cell lung cancer (Review). *Oncol Rep.* 2021;45(1):13–28.
5. Gravbrot N, Gilbert-Gard K, Mehta P, Ghotmi Y, Banerjee M, Mazis C, et al. Therapeutic Monoclonal Antibodies Targeting Immune Checkpoints for the Treatment of Solid Tumors. *Antibodies (Basel).* 2019;8(4).
6. Mielgo-Rubio X, Uribelarrea EA, Cortes LQ, Moyano MS. Immunotherapy in non-small cell lung cancer: Update and new insights. *J Clin Transl Res.* 2021;7(1):1–21.
7. Cascone T, William WN, Jr., Weissferdt A, Leung CH, Lin HY, Pataer A, et al. Neoadjuvant nivolumab or nivolumab plus ipilimumab in operable non-small cell lung cancer: the phase 2 randomized NEOSTAR trial. *Nat Med.* 2021;27(3):504–14.
8. Garon EB, Hellmann MD, Rizvi NA, Carcereny E, Leighl NB, Ahn MJ, et al. Five-Year Overall Survival for Patients With Advanced NonSmall-Cell Lung Cancer Treated With Pembrolizumab: Results From the Phase I KEYNOTE-001 Study. *J Clin Oncol.* 2019;37(28):2518–27.
9. Horvath L, Thienpont B, Zhao L, Wolf D, Pircher A. Overcoming immunotherapy resistance in non-small cell lung cancer (NSCLC) - novel approaches and future outlook. *Mol Cancer.* 2020;19(1):141.
10. Zheng X, Weigert A, Reu S, Guenther S, Mansouri S, Bassaly B, et al. Spatial Density and Distribution of Tumor-Associated Macrophages Predict Survival in Non-Small Cell Lung Carcinoma. *Cancer Res.* 2020;80(20):4414–25.
11. Wortman JC, He TF, Solomon S, Zhang RZ, Rosario A, Wang R, et al. Spatial distribution of B cells and lymphocyte clusters as a predictor of triple-negative breast cancer outcome. *NPJ Breast Cancer.* 2021;7(1):84.
12. Wang PC, Hu ZQ, Zhou SL, Yu SY, Mao L, Su S, et al. The spatial distribution of immune cell subpopulations in hepatocellular carcinoma. *Cancer Sci.* 2022;113(2):423–31.

13. Ge Z, Wu S, Zhang Z, Ding S. Mechanism of tumor cells escaping from immune surveillance of NK cells. *Immunopharmacol Immunotoxicol*. 2020;42(3):187–98.
14. Tang XY, Shi AP, Xiong YL, Zheng KF, Liu YJ, Shi XG, et al. Clinical Research on the Mechanisms Underlying Immune Checkpoints and Tumor Metastasis. *Front Oncol*. 2021;11:693321.
15. Reuben A, Zhang J, Chiou SH, Gittelman RM, Li J, Lee WC, et al. Comprehensive T cell repertoire characterization of non-small cell lung cancer. *Nat Commun*. 2020;11(1):603.
16. Lababede O, Meziane MA. The Eighth Edition of TNM Staging of Lung Cancer: Reference Chart and Diagrams. *Oncologist*. 2018;23(7):844–8.
17. Parra ER, Ferrufino-Schmidt MC, Tamegnon A, Zhang J, Solis L, Jiang M, et al. Immuno-profiling and cellular spatial analysis using five immune oncology multiplex immunofluorescence panels for paraffin tumor tissue. *Sci Rep*. 2021;11(1):8511.
18. Hernandez S, Rojas F, Laberiano C, Lazcano R, Wistuba I, Parra ER. Multiplex Immunofluorescence Tyramide Signal Amplification for Immune Cell Profiling of Paraffin-Embedded Tumor Tissues. *Front Mol Biosci*. 2021;8:667067.
19. Parra ER. Methods to Determine and Analyze the Cellular Spatial Distribution Extracted From Multiplex Immunofluorescence Data to Understand the Tumor Microenvironment. *Front Mol Biosci*. 2021;8:668340.
20. Becht E, McInnes L, Healy J, Dutertre CA, Kwok IWH, Ng LG, et al. Dimensionality reduction for visualizing single-cell data using UMAP. *Nat Biotechnol*. 2018.
21. Le Mercier I, Lines JL, Noelle RJ. Beyond CTLA-4 and PD-1, the Generation Z of Negative Checkpoint Regulators. *Front Immunol*. 2015;6:418.
22. Picarda E, Ohaegbulam KC, Zang X. Molecular Pathways: Targeting B7-H3 (CD276) for Human Cancer Immunotherapy. *Clin Cancer Res*. 2016.
23. Yu N, Li X, Zheng S, Li X. B7-H4's role "beyond the tumor". *Inflammation*. 2013;36(4):941–7.
24. Massari F, Santoni M, Ciccarese C, Santini D. The immunecheckpoints in modern oncology: the next 15 years. *Expert Opin Biol Ther*. 2015;15(7):917–21.
25. Linch SN, McNamara MJ, Redmond WL. OX40 Agonists and Combination Immunotherapy: Putting the Pedal to the Metal. *Front Oncol*. 2015;5:34.
26. Fu T, He Q, Sharma P. The ICOS/ICOSL pathway is required for optimal antitumor responses mediated by anti-CTLA-4 therapy. *Cancer Res*. 2011;71(16):5445–54.
27. Willoughby J, Griffiths J, Tews I, Cragg MS. OX40: Structure and function - What questions remain? *Mol Immunol*. 2017;83:13–22.
28. Croft M, So T, Duan W, Soroosh P. The significance of OX40 and OX40L to T-cell biology and immune disease. *Immunol Rev*. 2009;229(1):173–91.
29. Shi X, Wu S, Sun J, Liu Y, Zeng X, Liang Z. PD-L1 expression in lung adenosquamous carcinomas compared with the more common variants of non-small cell lung cancer. *Sci Rep*. 2017;7:46209.

30. Xia B, Herbst RS. Immune checkpoint therapy for non-small-cell lung cancer: an update. *Immunotherapy*. 2016;8(3):279–98.
31. Shen M, Ren X. Highlights on immune checkpoint inhibitors in non-small cell lung cancer. *Tumour Biol*. 2017;39(3):1010428317695013.
32. Schalper KA, Carvajal-Hausdorf D, McLaughlin J, Altan M, Velcheti V, Gaule P, et al. Differential Expression and Significance of PD-L1, IDO-1, and B7-H4 in Human Lung Cancer. *Clin Cancer Res*. 2017;23(2):370–8.
33. Brahmer JR. Immune checkpoint blockade: the hope for immunotherapy as a treatment of lung cancer? *Semin Oncol*. 2014;41(1):126–32.
34. Ceeraz S, Nowak EC, Burns CM, Noelle RJ. Immune checkpoint receptors in regulating immune reactivity in rheumatic disease. *Arthritis Res Ther*. 2014;16(5):469.
35. Kawase A, Yoshida J, Ishii G, Nakao M, Aokage K, Hishida T, et al. Differences between squamous cell carcinoma and adenocarcinoma of the lung: are adenocarcinoma and squamous cell carcinoma prognostically equal? *Jpn J Clin Oncol*. 2012;42(3):189–95.
36. Ma J, Xu H, Wang S. Immunosuppressive Role of Myeloid-Derived Suppressor Cells and Therapeutic Targeting in Lung Cancer. *J Immunol Res*. 2018;2018:6319649.
37. Li H, van der Leun AM, Yofe I, Lubling Y, Gelbard-Solodkin D, van Akkooi ACJ, et al. Dysfunctional CD8 T Cells Form a Proliferative, Dynamically Regulated Compartment within Human Melanoma. *Cell*. 2019;176(4):775–89 e18.
38. Sakaguchi S, Miyara M, Costantino CM, Hafler DA. FOXP3 + regulatory T cells in the human immune system. *Nat Rev Immunol*. 2010;10(7):490–500.
39. Bull JA, Macklin PS, Quaiser T, Braun F, Waters SL, Pugh CW, et al. Combining multiple spatial statistics enhances the description of immune cell localisation within tumours. *Sci Rep*. 2020;10(1):18624.
40. Artal Cortes A, Calera Urquizu L, Hernando Cubero J. Adjuvant chemotherapy in non-small cell lung cancer: state-of-the-art. *Transl Lung Cancer Res*. 2015;4(2):191–7.
41. Chesney JA, Mitchell RA, Yaddanapudi K. Myeloid-derived suppressor cells-a new therapeutic target to overcome resistance to cancer immunotherapy. *J Leukoc Biol*. 2017;102(3):727–40.
42. Solinas C, De Silva P, Bron D, Willard-Gallo K, Sangiolo D. Significance of TIM3 expression in cancer: From biology to the clinic. *Semin Oncol*. 2019;46(4–5):372–9.
43. Huang X, Zhang X, Li E, Zhang G, Wang X, Tang T, et al. VISTA: an immune regulatory protein checking tumor and immune cells in cancer immunotherapy. *J Hematol Oncol*. 2020;13(1):83.
44. Mantovani A, Allavena P, Sica A, Balkwill F. Cancer-related inflammation. *Nature*. 2008;454(7203):436–44.
45. Barua S, Fang P, Sharma A, Fujimoto J, Wistuba I, Rao AUK, et al. Spatial interaction of tumor cells and regulatory T cells correlates with survival in non-small cell lung cancer. *Lung Cancer*. 2018;117:73–9.

analysis software (Akoya Biosciences), and the chord diagram was generated using R studio software version 3.6.1.

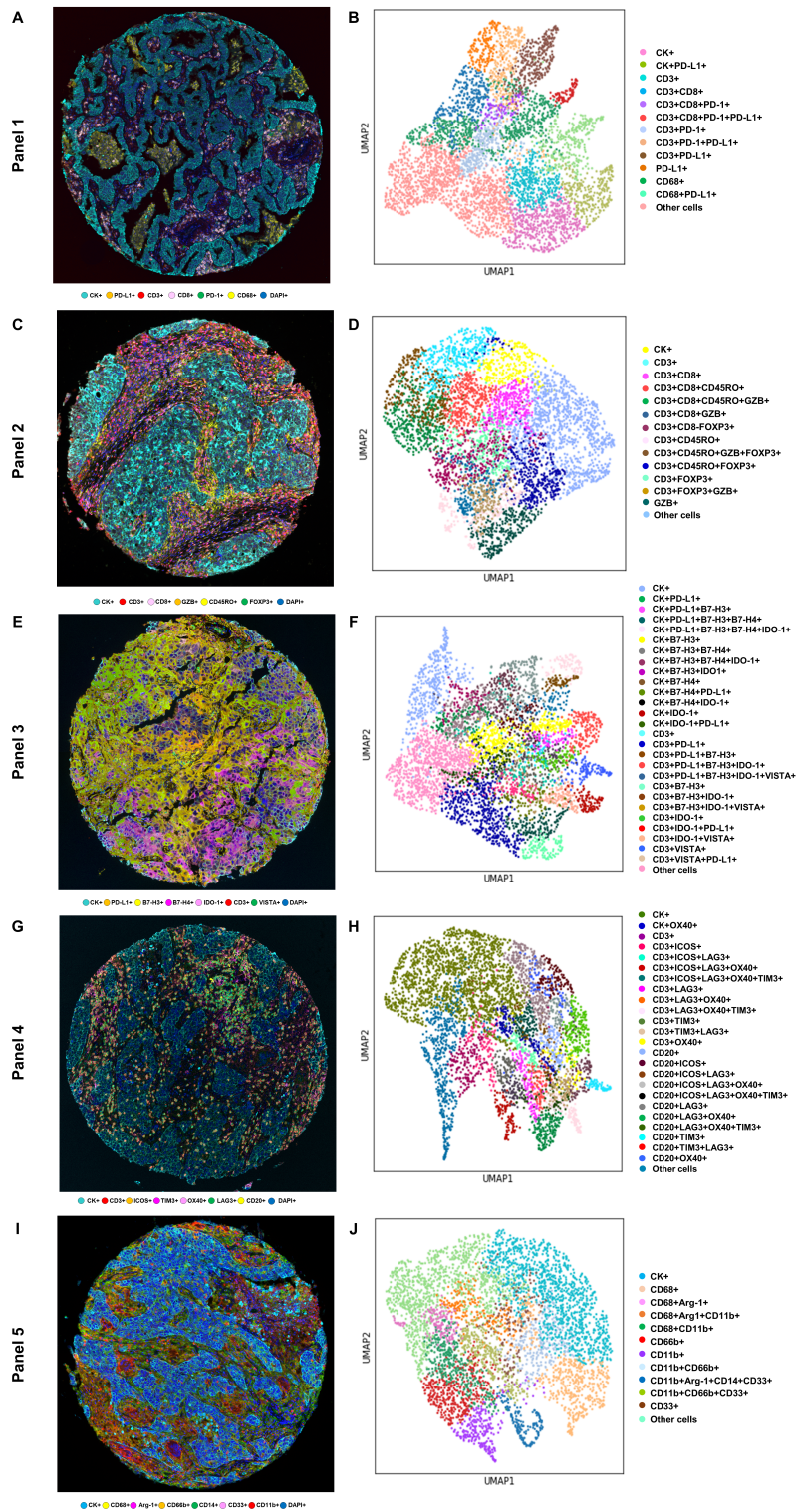


Figure 2

Representative examples of multispectral images and uniform manifold approximation and projection (UMAP) of clustering of cell types from non-small cell lung cancer tissue. Composite spectral mixing

images from multiplex immunofluorescence (mIF; 20× magnification) is shown colored marker co-expression for (A) panel 1, (C) panel 2, (E) panel 3, (G) panel 4 and, (I) panel 5. Color-coded UMAP visualizations show cell types identified by mIF panels: (B) 13 major cell types identified in panel 1, (D) 14 major cell types identified in panel 2, (F) 27 major cell types identified in panel 3, (H) 25 major cell types identified in panel 4, and (J) 12 major cell types identified in panel 5. The images were generated using Vectra-Polaris 3.0.3 scanner system and InForm 2.4.8 image analysis software (Akoya Biosciences) and, UMAP visualizations were generated using Python v.3.8.9, and the mIF images were generated using Vectra-Polaris 3.0.3 scanner system and InForm 2.4.8 image analysis software (Akoya Biosciences).

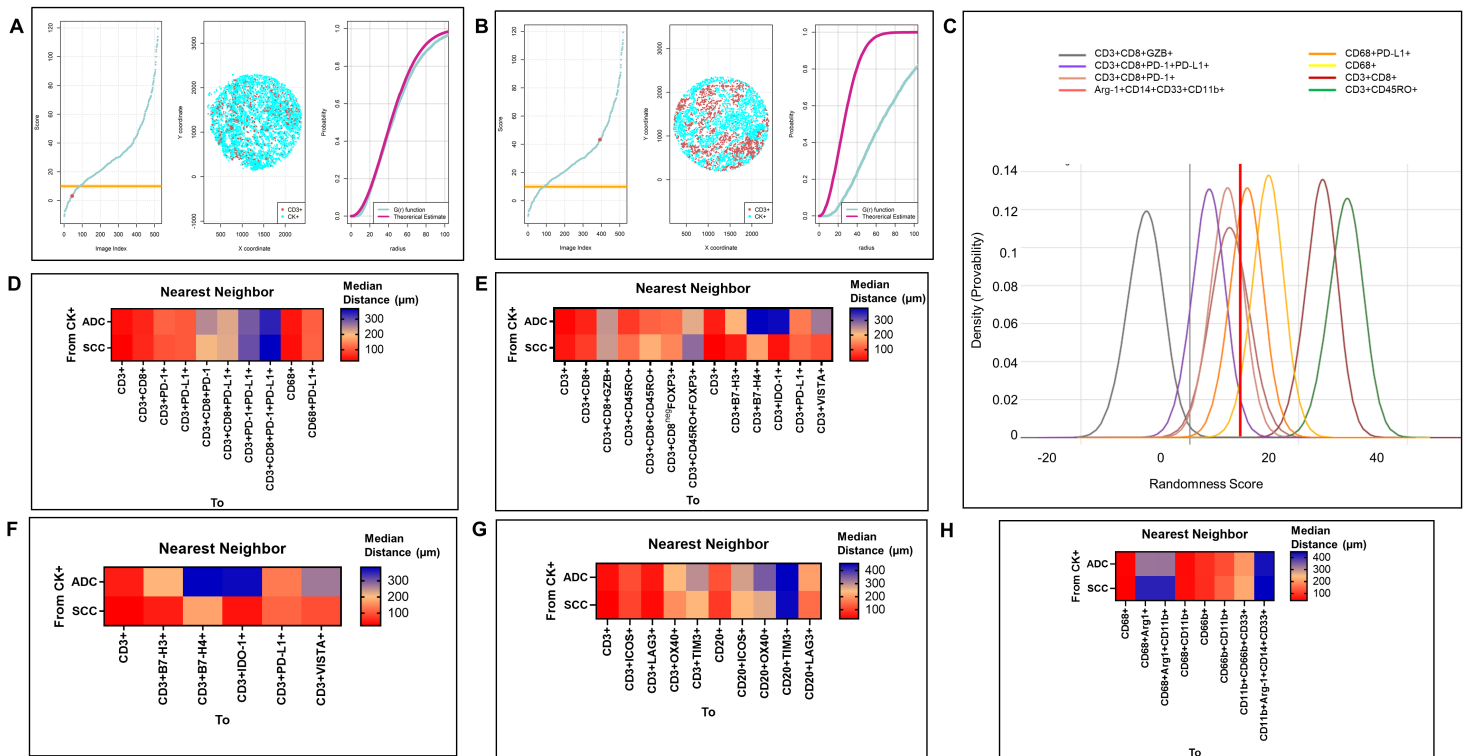


Figure 3

Nearest neighbor distance G function and theoretical Poisson curve score graphs showing different cellular patterns of distance from cytokeratin+ cells (malignant cells) to CD3+ T-cells and heat maps representing distance patterns by histologic type. (A-B) Scoring system across tissue specimens and threshold to be considered part of the mixed (A) or unmixed (B) pattern. Graphs represent the scoring system (left), point pattern distributions related to the major T-cell population (middle), and G function and theoretical Poisson curve area (right). (C) Model interaction based on the G function and theoretical Poisson curve score, showing two different groups of interaction between specific phenotypes and malignant cells. Cell phenotypes with a score of -10 to 10 were characterized as having a mixed/heterogeneous pattern indicating more interaction with malignant cells, and cell phenotypes with a score of >10 were characterized as having an unmixed/clustering pattern indicating less interaction with malignant cells. Distance heat maps representing the most common tumor-associated immune cells near

malignant cells (CK+) for each panel and histologic type for (D) show panel 1, (E) panel 2, (F) panel 3, (G) panel 4 and (H) panel 5. Graphs and heat maps were generated using R studio software version 3.6.1.

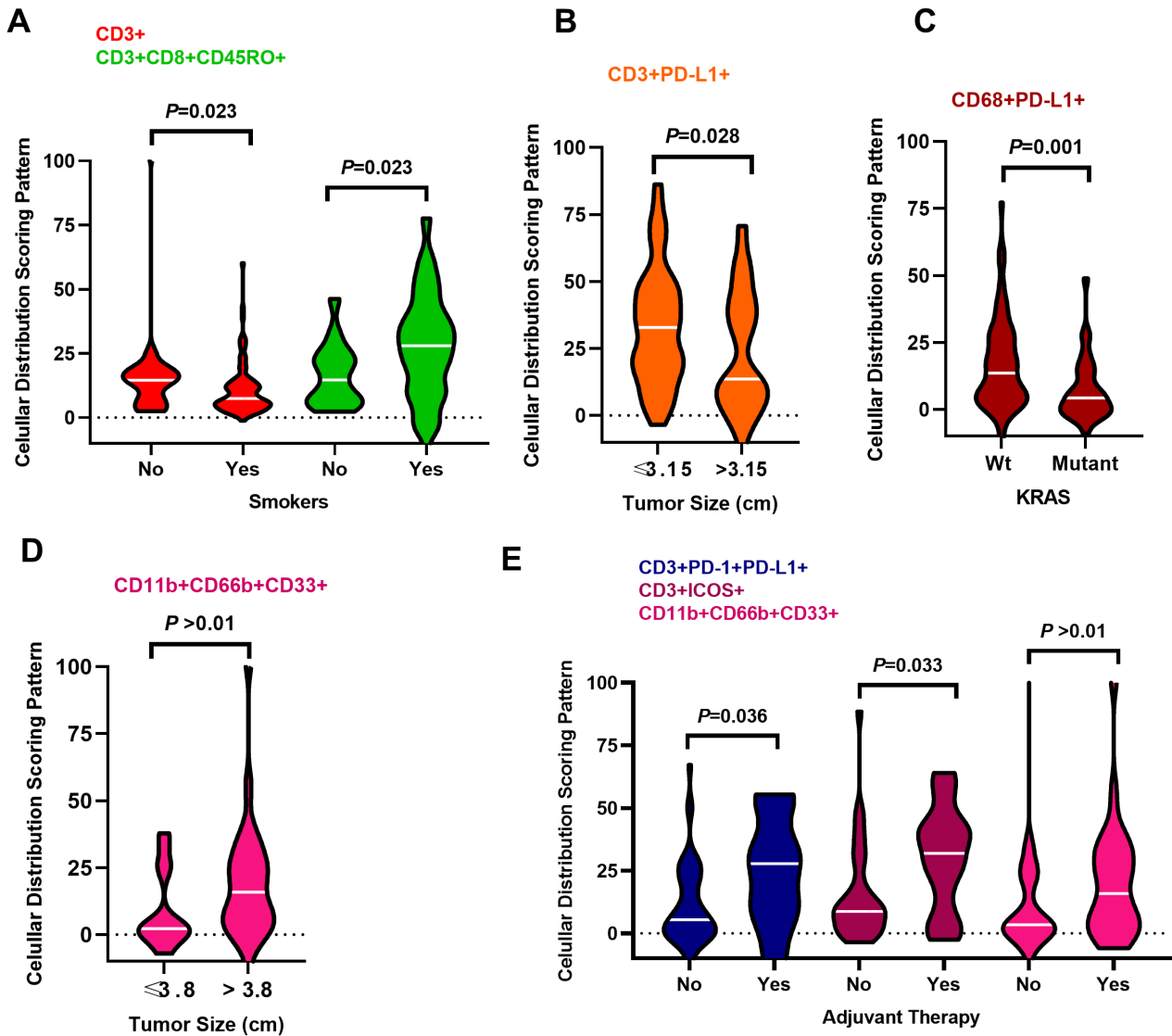


Figure 4

Violin plots showing associations between patterns of immune cell distribution and clinicopathologic features. Significant cellular distribution scoring patterns between immune cells and malignant cells are shown by (A) smoker status, (B) tumor size, and (C) *KRAS* mutation status for lung adenocarcinoma specimens. Significant cellular distribution scoring patterns between malignant cells and immune cells are shown by (D) tumor size and (E) adjuvant therapy for lung squamous cell carcinoma specimens. Graphs were generated using GraphPad Prism v.9.0.0.

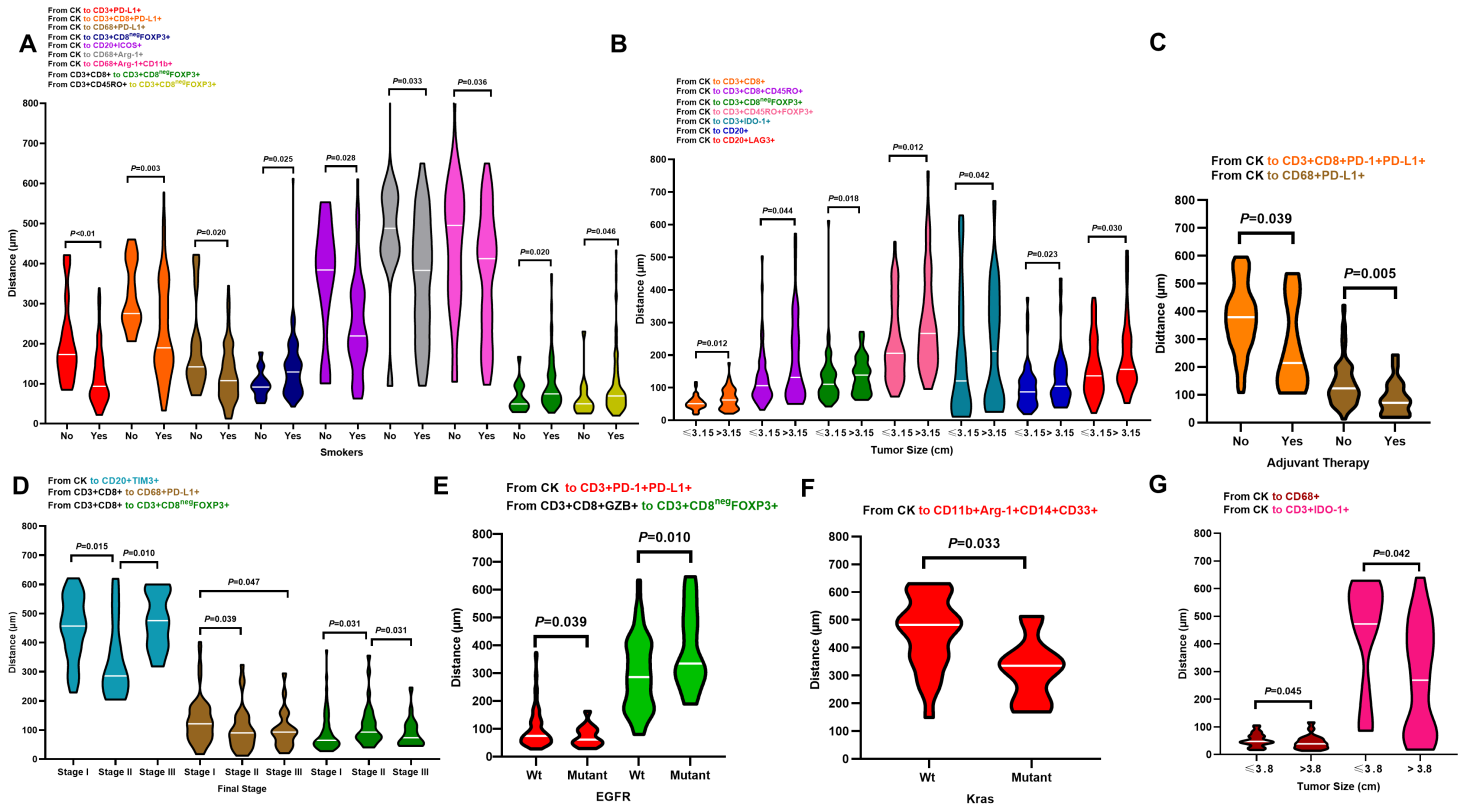


Figure 5

Violin plots showing associations between distances of immune cell populations from malignant cells and clinicopathologic features. Significant differences in distance between malignant cells and immune cells are shown by (A) smoker status, (B) tumor size, (C) adjuvant therapy, (D) final stage, and (E, F) mutation status in lung adenocarcinoma specimens. (G) Significant differences in distances between malignant cells and immune cells by tumor size are shown for lung squamous cell carcinoma specimens. Graphs were generated using GraphPad Prism v.9.0.0.

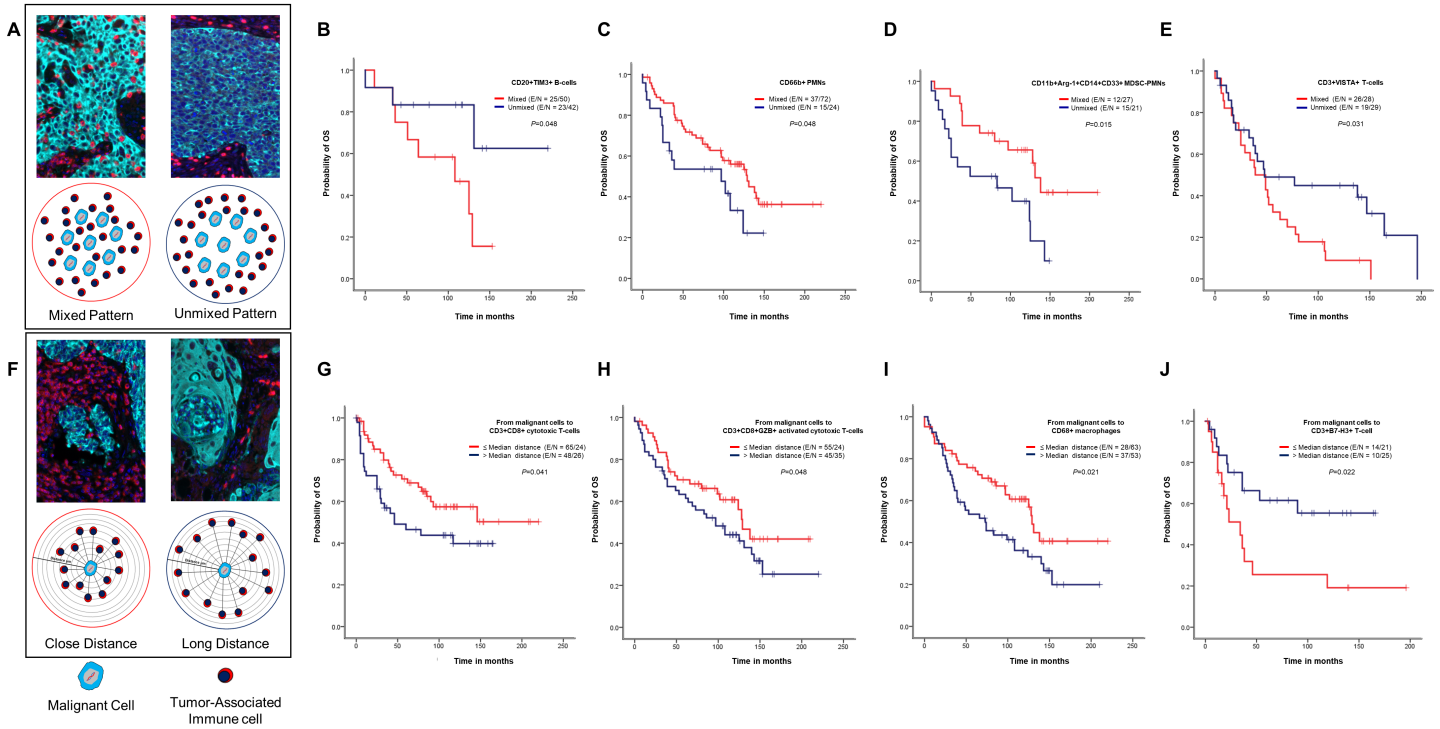


Figure 6

Kaplan-Meier analysis of overall survival (OS) by cellular patterns of distribution and distance from malignant cells to various immune cell subpopulations. (A) Composite spectral mixing images from multiplex immunofluorescence and illustration of the two different patterns of distribution, mixed and unmixed. Red lines indicate mixed pattern and blue lines indicate unmixed pattern between malignant cells and (B) CD20+TIM3+ B-cells, (C) CD66b+ granulocytes (PMNs), and (D) CD11b+Arg-1+CD14+CD33+ granulocytic myeloid-derived suppressor cells (MDSC-PMNs) in lung adenocarcinoma specimens and (E) CD3+VISTA+ T-cells in lung squamous cell carcinoma specimens. (F) Composite spectral mixing images from multiplex immunofluorescence and illustration of the distance metrics from malignant cells to different immune cells. Blue lines indicate long (>median) distances and red lines indicate close (\leq median) distances from malignant cells to (G) CD3+CD8+ cytotoxic T-cells, (H) CD3+CD8+GZB+ activated cytotoxic T-cells, (I) CD68+ macrophages, and (J) B7-H3+ T-cells in lung adenocarcinoma specimens. The images were generated using Vectra-Polaris 3.0.3 scanner system and InForm 2.4.8 image analysis software (Akoya Biosciences) and Kaplan-Meier curves were generated using R studio software version 3.6.0

Supplementary Files

This is a list of supplementary files associated with this preprint. Click to download.

- [SupplementaryFigure1.tif](#)
- [SupplementaryFigure2.tif](#)

- [SupplementaryFigure3.tif](#)
- [SupplementaryTable1.docx](#)
- [SupplementaryTable2.docx](#)
- [SupplementaryTable3.docx](#)
- [SupplementaryTable4.docx](#)
- [SupplementaryTable5.docx](#)
- [SupplementaryTable6.docx](#)
- [SupplementaryTable7.docx](#)